

# Macroscopic elastic properties of textured ZrN-AlN polycrystalline aggregates: From *ab initio* calculations to grain-scale interactions

D. Holec,<sup>1,\*</sup> F. Tasnádi,<sup>2</sup> P. Wagner,<sup>1</sup> M. Friák,<sup>3,4</sup> J. Neugebauer,<sup>3</sup> P. H. Mayrhofer,<sup>5</sup> and J. Keckes<sup>6,7</sup><sup>1</sup>*Department of Physical Metallurgy and Materials Testing, Montanuniversität Leoben, A-8700 Leoben, Austria*<sup>2</sup>*Department of Physics, Chemistry and Biology, Linköping University, SE-581 83 Linköping, Sweden*<sup>3</sup>*Max-Planck-Institut für Eisenforschung GmbH, D-40237 Düsseldorf, Germany*<sup>4</sup>*Institute of Physics of Materials, Academy of Sciences of the Czech Republic, v.v.i., CZ-61662 Brno, Czech Republic*<sup>5</sup>*Institute of Materials Science and Technology, Vienna University of Technology, A-1140 Vienna, Austria*<sup>6</sup>*Erich Schmid Institute of Materials Science, Austrian Academy of Sciences, A-8700 Leoben, Austria*<sup>7</sup>*Department of Materials Physics, Montanuniversität Leoben, A-8700 Leoben, Austria*

(Received 10 July 2014; revised manuscript received 1 September 2014; published 13 November 2014)

Despite the fast development of computational material modeling, the theoretical description of macroscopic elastic properties of textured polycrystalline aggregates starting from basic principles remains a challenging task. In this study we use a supercell-based approach to obtain the elastic properties of a random solid solution cubic  $\text{Zr}_{1-x}\text{Al}_x\text{N}$  system as a function of the metallic sublattice composition and texture descriptors. The employed special quasirandom structures are optimized not only with respect to short-range-order parameters, but also to make the three cubic directions  $[1\ 0\ 0]$ ,  $[0\ 1\ 0]$ , and  $[0\ 0\ 1]$  as similar as possible. In this way, only a small spread of elastic constant tensor components is achieved and an optimum trade-off between modeling of chemical disorder and computational limits regarding the supercell size and calculational time is proposed. The single-crystal elastic constants are shown to vary smoothly with composition, yielding  $x \approx 0.5$  an alloy constitution with an almost isotropic response. Consequently, polycrystals with this composition are suggested to have Young's modulus independent of the actual microstructure. This is indeed confirmed by explicit calculations of polycrystal elastic properties, both within the isotropic aggregate limit and with fiber textures with various orientations and sharpness. It turns out that for low AlN mole fractions, the spread of the possible Young's modulus data caused by the texture variation can be larger than 100 GPa. Consequently, our discussion of Young's modulus data of cubic  $\text{Zr}_{1-x}\text{Al}_x\text{N}$  contains also the evaluation of the texture typical for thin films.

DOI: [10.1103/PhysRevB.90.184106](https://doi.org/10.1103/PhysRevB.90.184106)

PACS number(s): 61.66.Dk, 62.20.D-, 71.15.Mb, 81.05.Je

## I. INTRODUCTION

Quantum mechanical calculations using density functional theory (DFT) of structural and elastic properties of materials have become a standard tool in modern computational material science. Recently, the alloying trends also have been extensively investigated, which in the area of hard protective coatings addressed predominantly issues related to the phase stability (see, e.g., Refs. [1–6]). This has been possible due to the increased computational power and the development of theories for treating random solid solutions. These include effective potential methods [7] (e.g., the coherent potential approximation or virtual coherent approximation), cluster methods [8,9] (e.g., the cluster expansion method), or supercell-based approaches, such as the special quasirandom structure (SQS) [10] technique employed in this paper. Practical advantages of using the supercell-based method include fast and easy generation of the supercells and direct insight into the local atomic environments; on other hand, the supercell size limits the concentration steps available, which is a serious limitation in particular for dilute alloys.

While the bulk modulus is relatively easy to obtain from the Birch-Murnaghan equation of state [11] as used during the structure optimization, the full tensor of elastic constants  $C_{ij}$  requires additional calculations. The two common methods to calculate  $C_{ij}$  from first principles are the total-energy method and the stress-strain method. The latter relies on the availability of the stress tensor and uses Hooke's law to evaluate  $C_{ij}$  directly. On the other hand, the total-energy method assigns an energy difference between a ground and a deformed state to the strain energy. This is a function of applied strain and a specific combination of the elastic constants. The advantage of this method is that the total energy is always available from *ab initio* calculations and it furthermore allows for estimation of higher-order elastic constants [12]. The disadvantage is that it usually takes more CPU resources than the stress-strain method as more deformation modes need to be applied. It has been also recently proposed that the stress-strain method is a more robust technique [13].

When it comes to the elastic constants of materials without any long-range periodicity, the supercell approach faces an apparent problem: On the one hand, the distribution of atoms on the lattice sites is required to be as random as possible to mimic solid solutions, hence often leading to supercells with only primitive symmetry (space group  $P1$ ). On the other hand, the material is expected to exhibit certain symmetry based on its underlying lattice, for example, the cubic symmetry of nitride coatings with the B1 (NaCl) structure. A combined *ab initio* and molecular dynamics study [14] has shown that when the supercell is large enough, the differences between

\*david.holec@unileoben.ac.at

macroscopically equivalent directions or deformation modes (e.g., tension in the  $x$ ,  $y$ , and  $z$  directions in the cubic systems) vanish. Although this is promising, the idea is not in line with the original purpose of SQSs, which was to simulate random alloys with supercells as small as possible. Moakher and Norris [15] provided a rigorous mathematical theory on how to project a tensor of elastic constants with an arbitrary symmetry onto a tensor with a desired crystallographic symmetry. This has been applied to the cubic  $\text{Ti}_{1-x}\text{Al}_x\text{N}$  system [16,17] with satisfactory agreement with available experimental data, however still requiring supercells with around 100 atoms and averaging over crystallographically equivalent directions.

In this work we investigate a possible trade-off between the randomness and the overall effective symmetry by introducing directionally optimized SQSs (DOSQSs) (a detailed description is given in Sec. II A) with the aim that the resulting tensor of elastic constants exhibits deviations as small as possible between the equivalent elastic constants. This in turn can lead to a significant reduction of computational resources by applying only a reduced set of deformations (similar to what is done to perfectly ordered and fully symmetric compounds; see, e.g., Ref. [12]). The second part of this work is devoted to establishing the impact of a texture on the elastic constants of the polycrystalline aggregate. This is an important step towards a quantitative comparison of theoretical and experimental data, as well as a theory-guided prediction of thin-film growth directions that provide extremal mechanical properties. Additional improvements towards modeling of real materials would be finite-temperature effects and inclusion of grain boundaries, neither of which is addressed here.

To assess the performance of the supercells developed here, we have chosen the cubic  $\text{Zr}_{1-x}\text{Al}_x\text{N}$  system (NaCl prototype,  $Fm\bar{3}m$  space group). It is an isovalent system with well investigated and widely used  $\text{Ti}_{1-x}\text{Al}_x\text{N}$ . Compared with  $\text{TiN}$ ,  $\text{ZrN}$  has a lower coefficient of friction and has been suggested to have better oxidation resistance [3,18]. Additionally, calculated elastic constants of this system have not yet been published and experimental values are only scarce.

## II. METHODS

### A. Supercells

Warren-Cowley short-range-order (SRO) parameters  $\alpha_j$  are commonly used to quantify randomness of an atom distribution on lattice sites. For binary alloys (or pseudobinary, e.g., where the mixing happens only on one sublattice, as in the case of  $\text{Zr}_{1-x}\text{Al}_x\text{N}$ ), they are calculated as [19]

$$\alpha_j = 1 - \frac{N_{AB}^j}{x_A x_B N M^j}, \quad (1)$$

where  $x_A$  and  $x_B$  ( $x_A + x_B = 1$ ) are the mole fractions of atoms  $A$  and  $B$ , respectively,  $N$  is the number of sites in the supercell,  $M^j$  is the site coordination in the  $j$ th-neighbor distance  $d_j$ , and  $N_{AB}^j$  is the total number of  $\{A, B\}$  pairs of atoms separated by the  $d_j$  (number of  $A$ - $B$  bonds of length  $d_j$ ). This definition implies that  $\alpha_j > 0$  and  $\alpha_j < 0$  correspond to the tendency for clustering and ordering, respectively, while  $\alpha_j = 0$  describes an ideal statistically random alloy. When constructing SQSs,

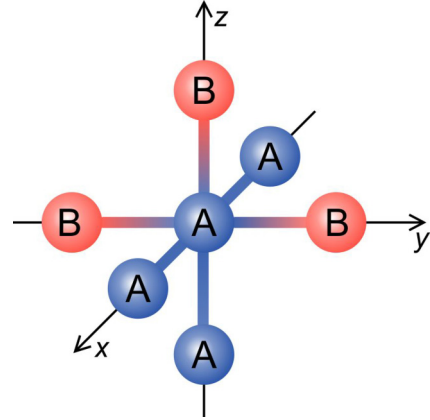


FIG. 1. (Color online) Schematic drawing of the DOSQS approach. The environment of the central atom  $A$  consists of two  $A$ - $A$  bonds in the  $x$  direction, two  $A$ - $B$  bonds in the  $y$  direction, and one  $A$ - $A$  and one  $A$ - $B$  bond in the  $z$  direction. The same environment is described as three  $A$ - $A$  and three  $A$ - $B$  bonds within the SQS approach.

the aim is to minimize values  $|\alpha_j|$  for several first coordination shells (typically between 5 and 7).

Tasnádi *et al.* [17] recently concluded that relatively large (around 100 atoms and more) supercells are needed to accurately describe the elastic response of cubic  $\text{Ti}_{0.5}\text{Al}_{0.5}\text{N}$ . Nevertheless, somewhat smaller cells with 64 atoms and overall cubic shape perform with acceptable accuracy too [17]. Moreover, we have applied the following additional constraint during the SQS generation: The number of bonds  $N_{AB}^j$  is divided into three subsets  $N_{AB,x}^j$ ,  $N_{AB,y}^j$ , and  $N_{AB,z}^j$ , depending on which projection of the vector  $AB$  in the  $x$ ,  $y$ , and  $z$  directions is the longest (Fig. 1). Since the three directions  $x$ ,  $y$ , and  $z$  are crystallographically equivalent in the cubic systems, the projected SRO parameters are calculated as

$$\alpha_{j,\xi} = 1 - \frac{N_{AB,\xi}^j}{\frac{1}{3} x_A x_B N M^j}, \quad \xi = x, y, z. \quad (2)$$

This way, the number of  $A$ - $B$  bonds is optimized with respect to the three equivalent directions. We applied this requirement also to the  $A$ - $A$  and  $B$ - $B$  bonds. The resulting supercells, hereafter called DOSQSs, are summarized in Table I. They were generated using a script that randomly distributes atoms  $A$  and  $B$  (considering a required chemical composition) on the (sub)lattice, hence providing a large ensemble of various atomic arrangements. For every one of them, projected SROs  $\alpha_{j,\xi}$  up to  $j = 5$  were evaluated and a supercell with  $\alpha_{j,\xi}$  closest to 0, i.e., an ideal solid solution, was chosen. The projected SROs of the resulting supercells are listed in Table II. It is worth noting that the compositions  $x = 0.125$  ( $x = 0.875$ ) and  $x = 0.375$  ( $= 0.625$ ) are worse optimized than the other two  $x = 0.25$  ( $x = 0.75$ ) and  $x = 0.5$ , a behavior consistent with the analysis of standard SQSs reported in Ref. [20]. Finally, although the DOSQS method is developed here for high-symmetry cubic systems, it can be applied also to other crystallographic classes by requesting the number of different bonds to be as similar as possible in equivalent directions.

TABLE I. Arrangement of atoms on the metallic sublattice in the supercells. An additional 32 positions according to the  $B1$  structure are occupied by N atoms. Compositions with  $x_A > 0.5$  are obtained by interchanging  $A$  and  $B$  atoms in a  $1 - x_A$  supercell.

Site coordinates			Mole fraction $x_A$			
$x$	$y$	$z$	0.125	0.25	0.375	0.5
0	0	0	$B$	$B$	$B$	$A$
0	0	0.5	$B$	$B$	$B$	$A$
0	0.25	0.25	$A$	$B$	$B$	$B$
0	0.25	0.75	$B$	$B$	$B$	$A$
0	0.5	0	$B$	$A$	$A$	$B$
0	0.5	0.5	$B$	$A$	$B$	$B$
0	0.75	0.25	$B$	$B$	$A$	$A$
0	0.75	0.75	$B$	$A$	$B$	$B$
0.25	0	0.25	$B$	$B$	$B$	$B$
0.25	0	0.75	$B$	$B$	$B$	$A$
0.25	0.25	0	$B$	$B$	$B$	$B$
0.25	0.25	0.5	$A$	$B$	$A$	$B$
0.25	0.5	0.25	$A$	$A$	$B$	$B$
0.25	0.5	0.75	$B$	$B$	$B$	$A$
0.25	0.75	0	$B$	$B$	$B$	$B$
0.25	0.75	0.5	$B$	$B$	$A$	$B$
0.5	0	0	$B$	$B$	$A$	$A$
0.5	0	0.5	$B$	$B$	$A$	$A$
0.5	0.25	0.25	$B$	$B$	$B$	$A$
0.5	0.25	0.75	$B$	$B$	$B$	$B$
0.5	0.5	0	$B$	$B$	$B$	$B$
0.5	0.5	0.5	$B$	$B$	$B$	$B$
0.5	0.75	0.25	$B$	$A$	$A$	$B$
0.5	0.75	0.75	$B$	$B$	$B$	$A$
0.75	0	0.25	$B$	$A$	$B$	$B$
0.75	0	0.75	$A$	$B$	$A$	$A$
0.75	0.25	0	$B$	$B$	$A$	$A$
0.75	0.25	0.5	$B$	$A$	$B$	$A$
0.75	0.5	0.25	$B$	$A$	$A$	$B$
0.75	0.5	0.75	$B$	$B$	$B$	$A$
0.75	0.75	0	$B$	$B$	$A$	$A$
0.75	0.75	0.5	$B$	$B$	$A$	$A$

### B. Elastic properties

The single-crystal elastic constants were obtained using the total-energy method, discussed in detail in Ref. [12]. The applied deformation matrices were

$$A1 = \begin{pmatrix} \delta & 0 & 0 \\ 0 & 0 & 0 \\ 0 & 0 & 0 \end{pmatrix}, \quad A2 = \begin{pmatrix} \delta & 0 & 0 \\ 0 & \delta & 0 \\ 0 & 0 & 0 \end{pmatrix}, \quad (3)$$

$$A4 = \begin{pmatrix} \delta & 0 & 0 \\ 0 & 0 & \delta \\ 0 & \delta & 0 \end{pmatrix}.$$

The volumetric density of the total-energy increase after application of such deformation matrix is, in the first approximation, a quadratic function of  $\delta$ ,

$$U_A(\delta) = \mathcal{A}\delta^2. \quad (4)$$

The coefficient  $\mathcal{A}$  depends on the applied deformation matrix  $A$ . For example, for  $A1$  it is equal to  $\frac{1}{2}C_{11}^{P1}$ . By changing

TABLE II. Directionally resolved SRO parameters calculated according to Eq. (2).

SRO parameter	Mole fraction $x_A$			
	0.125	0.25	0.375	0.5
$\alpha_{1,x}$	0.000	0.000	0.000	0.000
$\alpha_{1,y}$	0.000	0.000	0.000	0.000
$\alpha_{1,z}$	0.000	0.000	0.000	0.000
$\alpha_{2,x}$	-0.143	0.000	-0.067	0.000
$\alpha_{2,y}$	-0.143	0.000	-0.067	0.000
$\alpha_{2,z}$	-0.143	0.000	-0.067	0.000
$\alpha_{3,x}$	0.000	-0.083	-0.133	0.000
$\alpha_{3,y}$	-0.143	0.000	-0.133	0.000
$\alpha_{3,z}$	0.000	0.000	0.067	0.000
$\alpha_{4,x}$	-0.143	0.000	-0.067	0.000
$\alpha_{4,y}$	-0.143	-0.167	-0.067	0.000
$\alpha_{4,z}$	-0.143	-0.167	-0.067	0.000
$\alpha_{5,x}$	0.000	0.000	0.000	0.000
$\alpha_{5,y}$	0.000	0.000	0.000	0.000
$\alpha_{5,z}$	0.000	0.000	0.000	0.000

the position of the nonzero component  $\delta$  in the matrix  $A1$  to position (2,2) and (3,3), the coefficient  $\mathcal{A}$  changes to  $\frac{1}{2}C_{22}^{P1}$  and  $\frac{1}{2}C_{33}^{P1}$ , respectively. By fitting the  $U_A(\delta)$  curves for various deformation matrices (coefficients  $\mathcal{A}$  are listed in Table III), a full tensor  $C_{ij}^{P1}$  of single-crystal elastic constants was obtained for every composition. In doing so, the off-diagonal components for rows  $i = 4,5,6$  and for columns  $j = 4,5,6$  in  $C_{ij}^{P1}$  were set to 0.

Finally, application of the symmetry-based projection technique [15,21] as described in Ref. [17] yields the three cubic elastic constants  $C_{11}$ ,  $C_{12}$

TABLE III. Quadratic coefficient  $\mathcal{A}$  in the expansion of the strain energy (4) for various deformation matrices.

Deformation matrix	Position	$\mathcal{A}$
$A1$	(1,1)	$\frac{1}{2}C_{11}^{P1}$
$A1$	(2,2)	$\frac{1}{2}C_{22}^{P1}$
$A1$	(3,3)	$\frac{1}{2}C_{33}^{P1}$
$A2$	(1,1), (2,2)	$\frac{1}{2}(C_{11}^{P1} + C_{22}^{P1}) + C_{12}^{P1}$
$A2$	(1,1), (3,3)	$\frac{1}{2}(C_{11}^{P1} + C_{33}^{P1}) + C_{13}^{P1}$
$A2$	(2,2), (2,3)	$\frac{1}{2}(C_{22}^{P1} + C_{33}^{P1}) + C_{23}^{P1}$
$A4$	(1,1), (1,2), (2,1)	$\frac{1}{2}C_{11}^{P1} + 2C_{66}^{P1} + 2C_{16}^{P1}$
$A4$	(1,1), (1,3), (3,1)	$\frac{1}{2}C_{11}^{P1} + 2C_{55}^{P1} + 2C_{15}^{P1}$
$A4$	(1,1), (2,3), (3,2)	$\frac{1}{2}C_{11}^{P1} + 2C_{44}^{P1} + 2C_{14}^{P1}$
$A4$	(2,2), (1,2), (2,1)	$\frac{1}{2}C_{22}^{P1} + 2C_{66}^{P1} + 2C_{26}^{P1}$
$A4$	(2,2), (1,3), (3,1)	$\frac{1}{2}C_{22}^{P1} + 2C_{55}^{P1} + 2C_{25}^{P1}$
$A4$	(2,2), (2,3), (3,2)	$\frac{1}{2}C_{22}^{P1} + 2C_{44}^{P1} + 2C_{24}^{P1}$
$A4$	(3,3), (1,2), (2,1)	$\frac{1}{2}C_{33}^{P1} + 2C_{66}^{P1} + 2C_{36}^{P1}$
$A4$	(3,3), (1,3), (3,1)	$\frac{1}{2}C_{33}^{P1} + 2C_{55}^{P1} + 2C_{35}^{P1}$
$A4$	(3,3), (2,3), (3,2)	$\frac{1}{2}C_{33}^{P1} + 2C_{44}^{P1} + 2C_{34}^{P1}$

and  $C_{44}$ :

$$C_{11} = \frac{C_{11}^{P1} + C_{22}^{P1} + C_{33}^{P1}}{3}, \quad (5)$$

$$C_{12} = \frac{C_{12}^{P1} + C_{13}^{P1} + C_{23}^{P1}}{3}, \quad (6)$$

$$C_{44} = \frac{C_{44}^{P1} + C_{55}^{P1} + C_{66}^{P1}}{3}. \quad (7)$$

The anisotropy of the material is quantified using Zener's anisotropy ratio  $A$ :

$$A = \frac{2C_{44}}{C_{11} - C_{12}}. \quad (8)$$

The stress-strain method [22] was used to confirm the total-energy calculations of elastic constants. Additional tests were performed using a 96-atom  $4 \times 3 \times 4$  SQS supercell from Ref. [17].

The orientation distribution function (ODF)  $\mathcal{F}_{\text{ODF}}$  is a convenient way to quantify the texture of polycrystals. Here  $\mathcal{F}_{\text{ODF}}(\alpha, \beta, \gamma)$  is a function of three Euler angles  $\alpha$ ,  $\beta$ , and  $\gamma$  and for particular values it gives a fraction of grains with that orientation [23]. The Voigt's (constant strain in all grains) and Reuss's (constant stress in all grains) polycrystalline averages of elastic constants are defined as [24]

$$C_{ijkl}^V = \int_{\alpha, \beta, \gamma} \mathcal{F}_{\text{ODF}}(\alpha, \beta, \gamma) C_{ijkl}(\alpha, \beta, \gamma) d\alpha d\beta d\gamma, \quad (9)$$

$$(C^R)_{ijkl}^{-1} = \int_{\alpha, \beta, \gamma} \mathcal{F}_{\text{ODF}}(\alpha, \beta, \gamma) S_{ijkl}(\alpha, \beta, \gamma) d\alpha d\beta d\gamma, \quad (10)$$

where  $C_{ijkl}(\alpha, \beta, \gamma)$  and  $S_{ijkl}(\alpha, \beta, \gamma)$  are stiffness and compliance tensors, respectively, in a coordinate frame rotated by angles  $\alpha$ ,  $\beta$ , and  $\gamma$  with respect to the reference coordinate frame, in which both the ODF and the single crystal elastic constants are defined. In fact, Voigt's and Reuss's elastic averages represent the elastic response of a polycrystalline material with grain boundaries oriented parallel and perpendicular with respect to the applied stress direction. Single-valued polycrystalline elastic properties are obtained from Hill's average

$$C_{ijkl}^H = \frac{1}{2} (C_{ijkl}^V + C_{ijkl}^R). \quad (11)$$

A commercial package LABOTEX [25] was used to generate the ODFs describing the cubic fiber texture with preferred  $\langle 100 \rangle$  or  $\langle 111 \rangle$  orientation, different sharpness of the distribution [quantified by the full width at half maximum (FWHM) of the distribution [24]], and varying isotropic fraction.

### C. First-principles calculations

The quantum mechanical calculations within the framework of DFT were performed using the Vienna *ab initio* simulation package (VASP) [26,27]. The exchange and correlation effects were treated using the generalized gradient approximation as parametrized by Perdew, Burke, and Ernzerhof [28] and implemented in projector augmented wave pseudopotentials [29,30]. We used a plane-wave cutoff of 700 eV (500 eV) with a  $7 \times 7 \times 7$  ( $6 \times 6 \times 6$ ) Monkhorst-Pack  $k$ -point mesh for the 64- (96-) atom supercells, yielding a total-energy

accuracy on the order of meV. The slightly different parameter sets are a consequence of combining the results of two research groups; nevertheless, additional tests revealed that the changes in elastic constants induced by increasing the plane-wave cutoff energy from 500 to 700 eV and/or altering the  $k$  mesh are not larger than a few GPa. All supercells were fully structurally optimized yielding energies and lattice parameters as discussed in Ref. [31].

## III. RESULTS

### A. Single-crystal elastic constants

The single-crystal elastic constants calculated using the total-energy method as a function of the composition are shown in Fig. 2. Here  $C_{11}$ , describing the uniaxial elastic response, decreases from 522 GPa for ZrN to 377 GPa for  $\text{Zr}_{0.25}\text{Al}_{0.75}\text{N}$  and then increases again to 421 GPa for pure cubic AlN. On the contrary, off-diagonal shear-related components  $C_{12}$  and  $C_{44}$  increase with the AlN mole fraction from 118 GPa (ZrN) to 165 GPa (AlN) and from 105 GPa (ZrN) to 306 GPa (AlN), respectively. As a result, the Zener's anisotropy ratio  $A$  also increases monotonically with the AlN mole fraction. This corresponds to a qualitative change of the directional Young's modulus distribution: The stiffest direction is  $\langle 100 \rangle$  for ZrN and  $\langle 111 \rangle$  for AlN [12].

The error bars show standard deviation as obtained by averaging the three elastic constants equivalent for a perfect cubic material [17]. The relative error is below 3% for  $C_{11}$ , around 5% for  $C_{12}$ , and below 7% for  $C_{44}$  (with the exception of  $\text{Zr}_{0.5}\text{Al}_{0.5}\text{N}$ , where it is 11%). Consequently, one can in principle rely on values obtained only for deformation, e.g., in the  $x$  direction to get an estimate for the  $C_{11}$  with an accuracy better than 3% (a value usually regarded as an acceptable deviation between theory and experiment due to various exchange-correlation effects, temperature of measurement/calculation, material quality, etc. [32]).

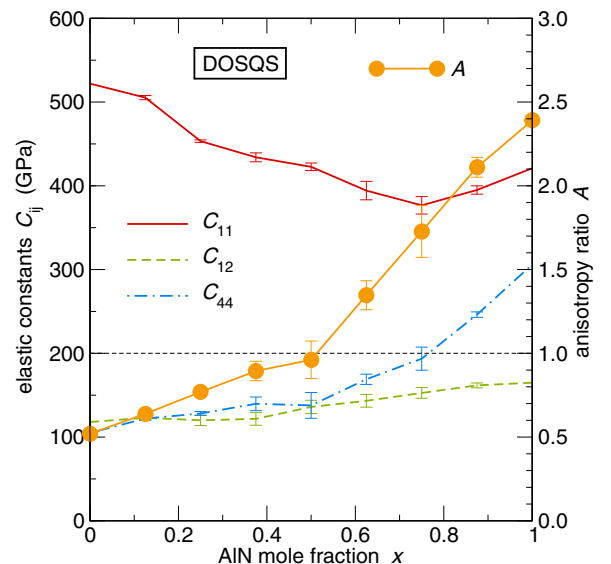


FIG. 2. (Color online) Single-crystal cubic elastic constants  $C_{11}$ ,  $C_{12}$ , and  $C_{44}$  and the Zener's anisotropy ratio  $A$  as functions of the AlN mole fraction in  $\text{Zr}_{1-x}\text{Al}_x\text{N}$ , calculated using the DOSQS approach.



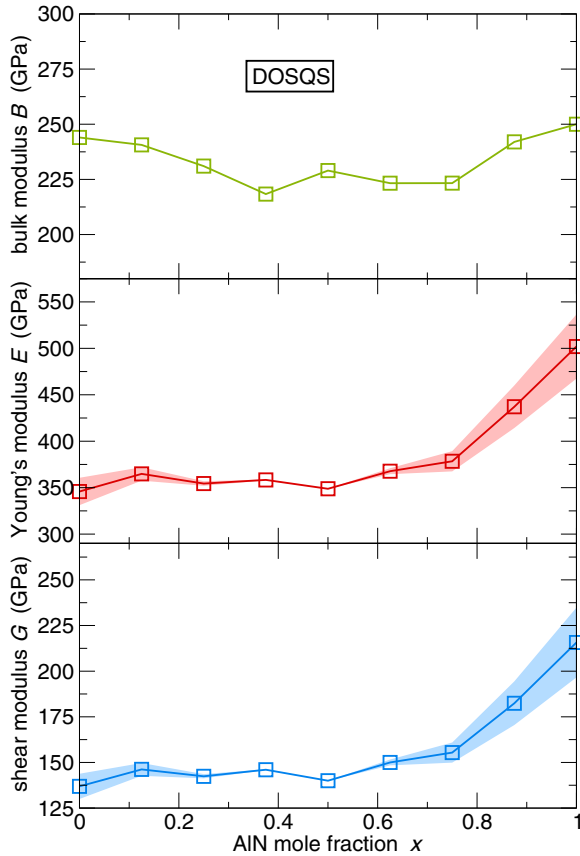


FIG. 3. (Color online) Bulk, Young's, and shear moduli for isotropic aggregates of  $\text{Zr}_{1-x}\text{Al}_x\text{N}$  grains as obtained using the DOSQS method. The shaded areas mark the spread of the respective quantities between Voigt's and Reuss's limits.

Zener's anisotropy ratio reaches 1 for  $\text{Zr}_{0.5}\text{Al}_{0.5}\text{N}$ , implying that for this composition the alloy should have an isotropic elastic response. This is a particularly interesting behavior, e.g., for a practical coating design. Generally, when deposition conditions are optimized to meet certain requirements such as grain size and shape, also the preferred orientation and consequently the elastic properties change. However, elastically isotropic materials exhibit an elastic response independent of the texture and hence such optimization would not influence the resulting mechanical properties. The range of isotropic elastic response of  $\text{Zr}_{1-x}\text{Al}_x\text{N}$  is further confirmed by evaluating the polycrystalline elastic constants in the following sections.

### B. Elastic response of isotropic polycrystal aggregates

We begin with presenting the polycrystalline properties of isotropic aggregates, i.e., when all crystal orientations are equally probable. Figure 3 shows the compositional dependence of the bulk modulus  $B$ , Young's modulus  $E$ , and the shear modulus  $G$ . The spread of the data as shown by the shaded area corresponds to the Voigt's (upper) and Reuss's (lower) limits. In the case of isotropic aggregates of cubic materials, i.e., when the ODF is a constant function, Eqs. (9)

and (10) simplify to [12]

$$G_V = \frac{C_{11} - C_{12} + 3C_{44}}{5}, \quad (12)$$

$$G_R = \frac{5}{4(S_{11} - S_{12}) + 3S_{44}}, \quad (13)$$

$$E_\alpha = \frac{9BG_\alpha}{3B + G_\alpha}, \quad (14)$$

where  $\alpha = V$  or  $R$  and  $S_{ij}$  are the elastic compliances corresponding to the elastic constants  $C_{ij}$  [33].

The bulk modulus changes only a little with the composition of  $\text{Zr}_{1-x}\text{Al}_x\text{N}$  and the alloy is predicted to be some 10% softer than the binary  $\text{ZrN}$  ( $B = 244$  GPa) and  $\text{AlN}$  ( $B = 250$  GPa);  $E$  and  $G$  exhibit the same behavior, being almost constant for  $\text{AlN}$  mole fractions up to  $x \approx 0.6$  and only then significantly rising. The range between Voigt's and Reuss's limits is largest for the binary nitrides and becomes almost zero for  $x \approx 0.4$ – $0.5$ . Hence for these compositions, the microstructure (lamellar or columnar) does not play a role for the resulting elastic response, as has been already stated in the previous section based on the Zener's anisotropy ratio.

### C. Influence of fiber texture

The elastic behavior of real materials with always unique microstructure is, however, different from that of isotropic polycrystalline aggregates. Hard ceramic coatings typically exhibit a  $\langle 100 \rangle$  or  $\langle 111 \rangle$  fiber texture [34], with a fiber axis oriented perpendicular to the substrate surface, which usually develops due to the minimization of the strain energy during nucleation or as a result of the surface/interface energy minimization, respectively. Hence we have investigated the influence of a particular fiber texture containing a certain fraction of isotropic background (isotropic aggregate of grains) on the elastic Young's modulus in a direction perpendicular to the film surface ( $z$  direction). The sharpness of the texture (width of the grain orientation distribution along the preferred orientation) is quantified by the FWHM parameter [24]. Figure 4 shows representative results of the Hill's average of Young's modulus in the  $z$  direction.

The values of the elastic constants for crystals with a FWHM equal to  $0.5^\circ$  and no isotropic background approach the single-crystal directional Young's modulus in the  $\langle 100 \rangle$  and  $\langle 111 \rangle$  directions, respectively. These values for  $\text{ZrN}$  ( $E_{\langle 100 \rangle} = 469$  GPa,  $E_{\langle 111 \rangle} = 307$  GPa) and  $\text{AlN}$  ( $E_{\langle 100 \rangle} = 338$  GPa,  $E_{\langle 111 \rangle} = 579$  GPa) exhibit the change of the softest (stiffest) direction from  $\langle 111 \rangle$  ( $\langle 100 \rangle$ ) for  $\text{ZrN}$  to  $\langle 100 \rangle$  ( $\langle 111 \rangle$ ) for  $\text{AlN}$ , as also shown earlier in Ref. [12].

An increase of the FWHM leads to a decrease (increase) of the Young's modulus in the  $z$  direction for  $\text{ZrN}$  with the  $\langle 100 \rangle$  ( $\langle 111 \rangle$ ) texture, as the contribution from softer (stiffer) oriented grains increases. A similar but opposite trend is obtained also for  $\text{AlN}$ . An increase of the isotropic content in the texture has qualitatively the same impact as an increasing FWHM (a decreasing sharpness of the texture). The Young's modulus values are independent of the FWHM parameter for 100% isotropic content since in these cases no texture fiber is present. Hence, also the values in the  $\langle 100 \rangle$  and  $\langle 111 \rangle$  plots

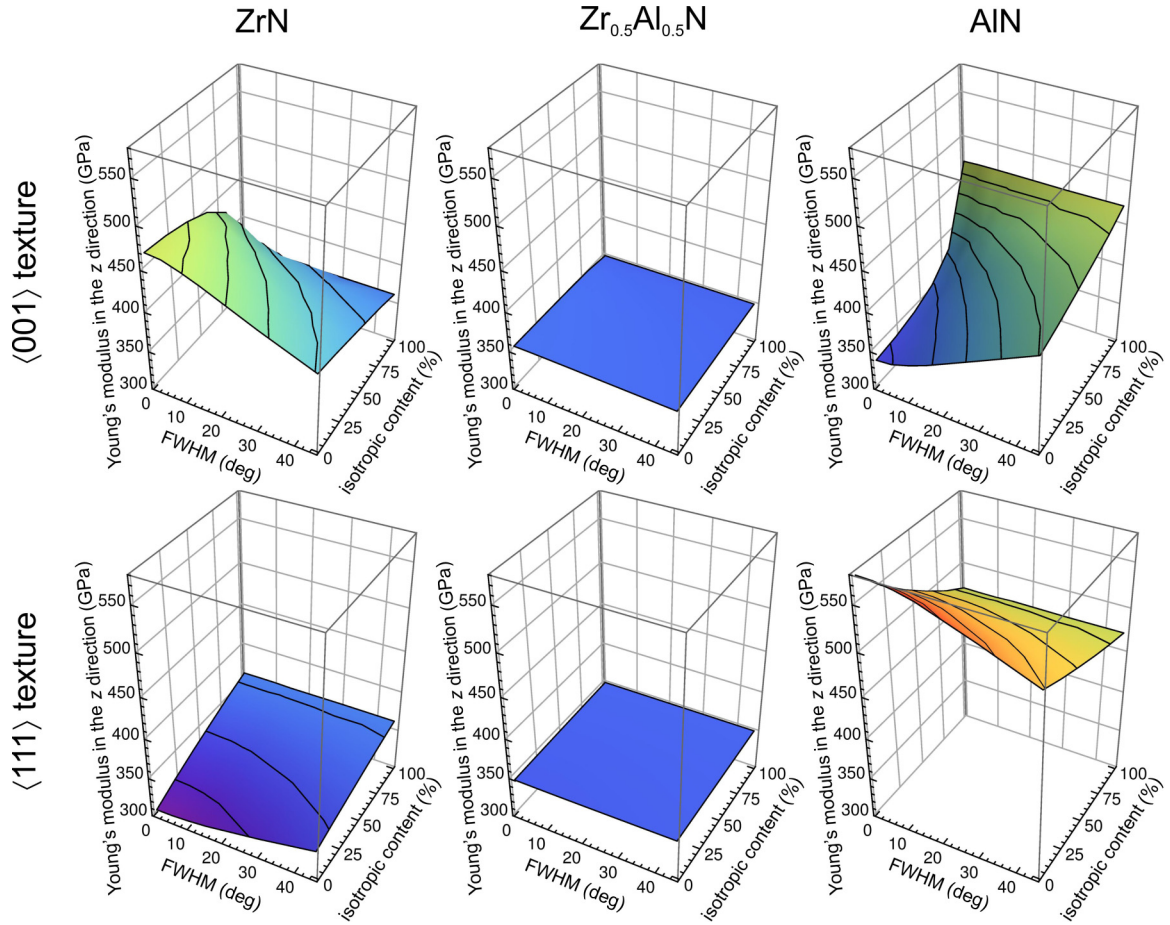


FIG. 4. (Color online) Dependence of the elastic response, as measured by Young's modulus in the  $z$  direction, on the texture sharpness (FWHM), content of the isotropic background, and alloy composition. The evaluation was done for fiber textures in the  $\langle 100 \rangle$  and  $\langle 111 \rangle$  directions.

are the same for 100% isotropic texture and correspond to the values shown in Fig. 3.

The shape of Young's modulus profile changes continuously with the composition. It is worth noting that for  $x = 0.5$ , an almost flat dependence is obtained. This underlines our earlier estimates that the elastic response of a  $\text{Zr}_{1-x}\text{Al}_x\text{N}$  solid solution around this composition is isotropic and independent of the texture (assuming that the grain boundary influence is negligible). To illustrate the compositional dependence further, we plotted in Fig. 5 the spread between the single-crystal Young's moduli in the  $\langle 100 \rangle$  and  $\langle 111 \rangle$  directions. It follows that the elastic response is most sensitive to the texture for the binary  $\text{ZrN}$  and  $\text{AlN}$ . Both theory [3,31] and experiment [35–37] suggest that the maximum AlN mole fraction in a supersaturated cubic single phase is about  $x \approx 0.4$ . Consequently, it can be stated that the addition of Al into  $\text{ZrN}$  up to its solubility limit results in the solid solution becoming steadily more elastically isotropic, hence decreasing the impact of film microstructure on the elastic behavior.

#### IV. DISCUSSION

##### A. Supercell size and the method used

A complementary calculation of the elastic constants have been performed in order to critically assess the quality of

the data presented here. The results obtained with standard but larger supercells (96-atom  $4 \times 3 \times 4$  supercells based on the fcc unit cell [17]) are shown together with the previously discussed elastic constants in Fig. 6. It follows that there is up to  $\approx 13\%$  difference in the  $C_{11}$  values, while the  $C_{12}$  and  $C_{44}$  are practically unchanged. As a consequence, the SQS-based calculation predicts Zener's anisotropy ratio  $A$  to be significantly higher than the value based on the DOSQS supercell. A test calculation using the DOSQS and the stress-strain method yields the same result as the total-energy approach applied to the DOSQS. Another test calculation using an ordinary 64-atom SQS cell yielded  $C_{11} \approx 2\%$  smaller than the corresponding DOSQS value. It can therefore be concluded that the discrepancies shown in Fig. 6 originate from the different supercell sizes (and shapes). This is similar to the behavior of an isovalent system  $\text{Ti}_{1-x}\text{Al}_x\text{N}$ , where  $C_{11}$  from the 64-atom supercell is about 7.5% smaller than the corresponding value calculated using a 96-atom supercell.

Moreover, the 96-atom SQS data shown are  $C_{11}^{P1}$ ,  $C_{12}^{P1}$ , and  $C_{44}^{P1}$  instead of the projected elastic constants  $C_{11}$ ,  $C_{12}$ , and  $C_{44}$  [for which nine elastic constants would be needed; see Eqs. (5)–(7)]. As shown in Ref. [17], when only  $C_{11}^{P1}$ ,  $C_{12}^{P1}$ , and  $C_{44}^{P1}$  are used to calculate  $A$  (a value labeled  $A_x$ ),  $A_x$  is overestimated by  $\approx 18\%$  with respect to the value  $A$  based on the projected elastic constants for  $x = 0.5$ . The other set

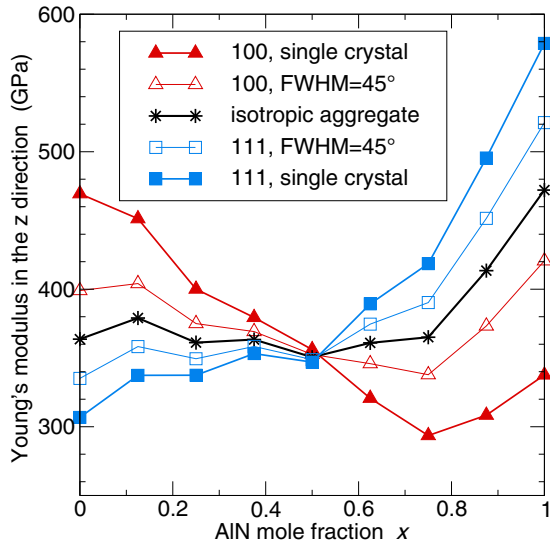


FIG. 5. (Color online) Compositional dependence of Young's modulus for various textures as a function of AlN mole fraction. These data were calculated using the DOSQS cells and suggest  $x \approx 0.5$  to be the texture-independent composition.

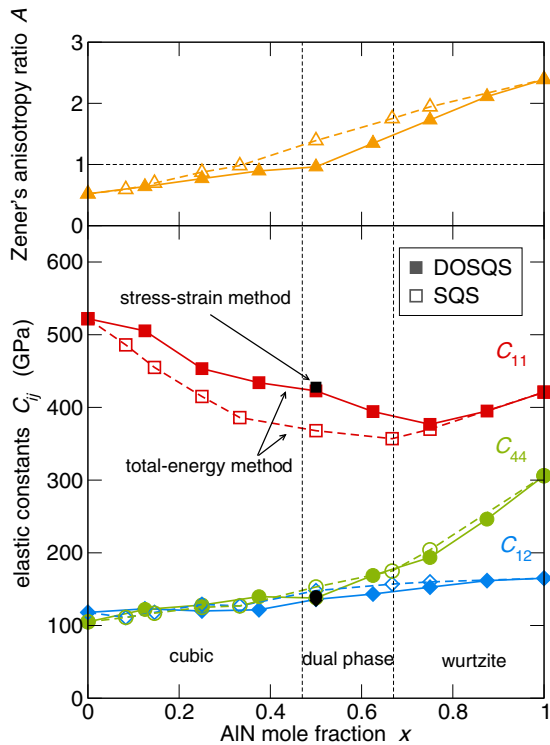


FIG. 6. (Color online) Overview of the supercell size and calculation method impact on the predicted single-crystal elastic constants as functions of the  $\text{Zr}_{1-x}\text{Al}_x\text{N}$  alloy composition. The elastic constants  $C_{11}$ ,  $C_{12}$ , and  $C_{44}$  are represented by squares, diamonds, and circles, respectively, while triangles are used for Zener's anisotropy ratio  $A$ . Closed and open symbols correspond to DOSQS and SQS cells, respectively. The small black symbols represent results obtained from the stress-strain method; all other data points were calculated using the total energy method.

of elastic constants  $C_{22}^{P1}$ ,  $C_{23}^{P1}$ , and  $C_{55}^{P1}$  ( $A_y$ ) and  $C_{33}^{P1}$ ,  $C_{13}^{P1}$ , and  $C_{66}^{P1}$  ( $A_z$ ) underestimate  $A$  by 9% and 7%, respectively. In contrast, the DOSQS results in a significantly reduced spread of the Zener's ratio. For example, for  $x = 0.5$  our data yield  $A_x/A = 1.026$ ,  $A_y/A = 0.997$ , and  $A_z/A = 0.978$ . A similar trend was observed also for the standard 64-atom SQS in Ref. [17].

The supercell size and using/not using the projection technique for  $C_{ij}$  add up and cause the Zener's anisotropy ratio  $A$  of the 96-atom supercell to increase more steeply (than the DOSQS value) for low AlN mole fractions, yielding  $x \approx 0.35$  as the composition with the nearly isotropic response. As a consequence of the overestimated  $A$  for the 96-atom SQS, the isotropic concentration is expected to be shifted to higher Al concentrations in Fig. 6, hence get closer to the DOSQS predictions, when the corrected projected  $C_{ij}$  values are used. It can therefore be concluded that the DOSQS cells proposed here are more appropriate for a direct estimation of  $C_{ij}$  (i.e., without projecting the nine  $P1$  values on the three cubic  $C_{11}$ ,  $C_{12}$ , and  $C_{44}$ ) than the 96-atom SQS supercell.

Focusing on the single-crystal elastic constants for compositions  $x < 0.4$  (i.e., those experimentally accessible in a single phase), the relative error from averaging  $C_{11}$  from deformations in the  $x$ ,  $y$ , and  $z$  directions is a maximum  $\approx 1\%$ , while it is below  $\approx 6\%$  for  $C_{12}$  and  $C_{44}$ .<sup>1</sup> When such accuracy is acceptable, the DOSQSs proposed here can be used to perform only one of the three symmetry equivalent deformations (i.e.,  $x$ ,  $y$ , or  $z$  for  $C_{11}$ ) to obtain the respective elastic constant of the alloy.

The off-diagonal components in rows  $i = 4, 5, 6$  and columns  $j = 4, 5, 6$  set to 0 GPa during the fitting procedure of the total-energy method were confirmed to be negligibly small (below 3 GPa) using the stress-strains method. Therefore, the assumption used does not influence our results.

As pointed out in recent publications (see, e.g., Refs. [13,38]), the stress-strain method proves to be more robust than the total-energy approach. It is also faster as one deformation yields several linearly independent equations for obtaining the full  $6 \times 6$  matrix of elastic constants. It follows that the stress-strain method performed on a standard SQS (possibly with more atoms) should be the preferred method. When a reliable interatomic potential exists, a molecular-dynamics-based approach on large SQSs [14] may be an acceptable approach. However, in the case when neither the stress tensor nor the good non-DFT-based method is available, we propose that our DOSQSs together with the total-energy method are a suitable (CPU-time affordable) approach.

## B. Comparison with experimental data

There are only a few experimental reports on the mechanical properties of  $\text{Zr}_{1-x}\text{Al}_x\text{N}$  monolithic films in the literature. Lamni *et al.* [37] reported on magnetron sputtered thin films

<sup>1</sup>This is likely to be related to the way DOSQS cells are constrained during their generation. To decrease the spread between, e.g.,  $C_{12}$ ,  $C_{13}$ , and  $C_{23}$ , additional cubic symmetries have to be considered during the cell construction.

that keep the cubic structure up to an AlN mole fraction  $x = 0.43$ . The films have the preferred  $\langle 111 \rangle$  texture. The Young's modulus, as measured by nanoindentation, increases from 250 GPa for pure ZrN to 300 GPa for  $\text{Zr}_{0.57}\text{Al}_{0.43}\text{N}$ . The predicted Young's modulus for the preferred  $\langle 111 \rangle$  texture increases from 307 GPa (335 GPa) for ZrN to 389 GPa (375 GPa) for  $\text{Zr}_{0.625}\text{Al}_{0.375}\text{N}$  for a FWHM equal to  $0.5^\circ$  ( $45^\circ$ ) (compare with Fig. 5). Therefore, the trend, as well as the magnitude of the increase, is correctly predicted by our calculations. The somewhat softer Young's modulus experimentally is likely to be related to the presence of grain boundaries in the real microstructure as well as finite temperature during experimental measurement. The same authors also published a value of the nanoindented Young's modulus of 250 GPa for the as-deposited  $\text{Zr}_{0.57}\text{Al}_{0.43}\text{N}$  [39], which increased to 265 GPa after annealing the sample to  $850^\circ\text{C}$ . Rogström *et al.* [36] also observed an increase in Young's modulus after annealing their arc-deposited  $\text{Zr}_{0.52}\text{Al}_{0.48}\text{N}$  to  $1400^\circ\text{C}$  and argued that this was a consequence of an increased grain size, a decreased porosity, and an improved crystallinity of their sample. Although the grain size is not reflected in our calculations (the ODF takes into account only the grain orientations, not their size nor shape), its effect, i.e., decreasing the volume fraction of the soft grain boundaries, can be intuitively foreseen. It therefore further underlines the importance of the grain boundaries (as well as the amorphous matrix present in the case of  $\text{Zr}_{1-x}\text{Al}_x\text{N}$ ) on the mechanical properties of nanocrystalline materials. This topic cannot be easily handled by means of density functional theory itself and would require use of multimethod scale-bridging techniques (see, e.g., [40,41]).

Nevertheless, the influence of the grain boundary fraction has been experimentally proven by our results for reactively prepared  $\text{Zr}_{0.65}\text{Al}_{0.35}\text{N}$  and nonreactively prepared  $\text{Zr}_{0.68}\text{Al}_{0.32}\text{N}$  coatings possessing a single-phase cubic structure and a mixed  $\langle 111 \rangle$ - $\langle 200 \rangle$  orientation. The reactively prepared coatings have a grain size of 8 nm and a Young's modulus of 347 GPa, whereas the nonreactively prepared coatings have a grain size of 36 nm and also a larger Young's

modulus of 398 GPa [42]. The latter is in almost perfect agreement with our calculations for  $\text{Zr}_{0.625}\text{Al}_{0.375}\text{N}$  with a FWHM of  $0.5^\circ$  yielding 389 GPa.

## V. CONCLUSION

The directionally optimized SQSs proposed here seem to be a reasonable alternative to large standard SQSs for the estimation of elastic properties of alloys, in particular for systems with cubic symmetry. When well optimized, they can provide accurate single-crystal elastic constants while significantly reducing the number of calculations needed by omitting the need for symmetry-based projection of  $C_{ij}$ .

Based on the calculated single-crystal elastic constants, we proposed that  $\text{Zr}_{1-x}\text{Al}_x\text{N}$  with an AlN mole fraction  $x \approx 0.4$ – $0.5$  exhibits isotropic elastic behavior. This in particular means that any polycrystal with this composition will have a texture-independent Young's modulus. This hypothesis has been supported by explicitly evaluating the compositional dependence of Young's modulus on fiber texture orientation, its sharpness, and the amount of isotropic background. The comparison with experimental data showed decent agreement with our theoretically predicted values. The small discrepancy was ascribed mainly to the influence of grain boundaries. This phenomenon, however, goes beyond the capabilities of DFT and requires a multiscale/multimethod approach.

## ACKNOWLEDGMENTS

D.H. and P.H.M. greatly acknowledge financial support from the START Program (Y371) of the Austrian Science Fund (FWF), as well as the CPU time at the Vienna Scientific Cluster. M.F. acknowledges financial support from the Academy of Sciences of the Czech Republic through the Fellowship of Jan Evangelista Purkyně and access to the computational resources provided by the MetaCentrum under the program LM2010005 and the CERIT-SC under the program Centre CERIT Scientific Cloud, part of the Operational Program Research and Development for Innovations, Reg. No. CZ.1.05/3.2.00/08.0144.

- 
- [1] P. H. Mayrhofer, D. Music, and J. M. Schneider, *J. Appl. Phys.* **100**, 094906 (2006).
  - [2] B. Alling, T. Marten, I. A. Abrikosov, and A. Karimi, *J. Appl. Phys.* **102**, 044314 (2007).
  - [3] S. H. Sheng, R. F. Zhang, and S. Veprek, *Acta Mater.* **56**, 968 (2008).
  - [4] G. M. Matenoglou, C. E. Lekka, L. E. Koutsokeras, G. Karras, C. Kosmidis, G. A. Evangelakis, and P. Patsalas, *J. Appl. Phys.* **105**, 103714 (2009).
  - [5] D. G. Sangiovanni, L. Hultman, and V. Chirita, *Acta Mater.* **59**, 2121 (2011).
  - [6] D. Holec, L. Zhou, R. Rachbauer, and P. H. Mayrhofer, *J. Appl. Phys.* **113**, 113510 (2013).
  - [7] A. Gonis, *Theoretical Materials Science: Tracing the Electronic Origins of Materials Behavior* (Materials Research Society, Warrendale, PA, 2000).
  - [8] J. M. Sanchez, *Phys. Rev. B* **81**, 224202 (2010).
  - [9] S. B. Maisel, M. Höfler, and S. Müller, *Nature (London)* **491**, 740 (2012).
  - [10] S.-H. Wei, L. G. Ferreira, J. E. Bernard, and A. Zunger, *Phys. Rev. B* **42**, 9622 (1990).
  - [11] F. Birch, *Phys. Rev.* **71**, 809 (1947).
  - [12] D. Holec, M. Friák, J. Neugebauer, and P. H. Mayrhofer, *Phys. Rev. B* **85**, 064101 (2012).
  - [13] M. A. Caro, S. Schulz, and E. P. O'Reilly, *J. Phys.: Condens. Matter* **25**, 025803 (2013).
  - [14] J. von Pezold, A. Dick, M. Friák, and J. Neugebauer, *Phys. Rev. B* **81**, 094203 (2010).
  - [15] M. Moakher and A. N. Norris, *J. Elast.* **85**, 215 (2006).
  - [16] F. Tasnádi, I. A. Abrikosov, L. Rogström, J. Almer, M. P. Johansson, and M. Odén, *Appl. Phys. Lett.* **97**, 231902 (2010).
  - [17] F. Tasnádi, M. Odén, and I. A. Abrikosov, *Phys. Rev. B* **85**, 144112 (2012).



- [18] L. Chen, D. Holec, Y. Du, and P. H. Mayrhofer, *Thin Solid Films* **519**, 5503 (2011).
- [19] S. Müller, *J. Phys.: Condens. Matter* **15**, R1429 (2003).
- [20] B. Alling, A. V. Ruban, A. Karimi, O. E. Peil, S. I. Simak, L. Hultman, and I. A. Abrikosov, *Phys. Rev. B* **75**, 045123 (2007).
- [21] J. Z. Liu, A. van de Walle, G. Ghosh, and M. Asta, *Phys. Rev. B* **72**, 144109 (2005).
- [22] R. Yu, J. Zhu, and H. Ye, *Comput. Phys. Commun.* **181**, 671 (2010).
- [23] H. J. Bunge, *Texture Analysis in Materials Science: Mathematical Methods* (Butterworths, Oxford, 1982).
- [24] K. J. Martinschitz, R. Daniel, C. Mitterer, and J. Keckes, *J. Appl. Crystallogr.* **42**, 416 (2009).
- [25] LABOTEX, Version 3.0 (LaboSoft, Krakow, 2006), <http://www.labosoft.com.pl/>.
- [26] G. Kresse and J. Hafner, *Phys. Rev. B* **47**, 558 (1993).
- [27] G. Kresse and J. Furthmüller, *Phys. Rev. B* **54**, 11169 (1996).
- [28] J. P. Perdew, K. Burke, and M. Ernzerhof, *Phys. Rev. Lett.* **77**, 3865 (1996).
- [29] P. E. Blöchl, *Phys. Rev. B* **50**, 17953 (1994).
- [30] G. Kresse and D. Joubert, *Phys. Rev. B* **59**, 1758 (1999).
- [31] D. Holec, R. Rachbauer, L. Chen, L. Wang, D. Luef, and P. H. Mayrhofer, *Surf. Coat. Technol.* **206**, 1698 (2011).
- [32] M. Friák, T. Hickel, B. Grabowski, L. Lymperakis, A. Udyansky, A. Dick, D. Ma, F. Roters, L.-F. Zhu, A. Schlieter, U. Kühn, Z. Ebrahimi, R. A. Lebensohn, D. Holec, J. Eckert, H. Emmerich, D. Raabe, and J. Neugebauer, *Eur. Phys. J. Plus* **126**, 1 (2011).
- [33] J. Nye, *Physical Properties of Crystals*, 1st ed. (Clarendon, Oxford, 1957).
- [34] P. H. Mayrhofer, C. Mitterer, L. Hultman, and H. Clemens, *Prog. Mater. Sci.* **51**, 1032 (2006).
- [35] H. Hasegawa, M. Kawate, and T. Suzuki, *Surf. Coat. Technol.* **200**, 2409 (2005).
- [36] L. Rogström, M. Ahlgren, J. Almer, L. Hultman, and M. Odén, *J. Mater. Res.* **27**, 1716 (2012).
- [37] R. Lamni, R. Sanjines, M. Parlinska-Wojtan, A. Karimi, and F. Levy, *J. Vac. Sci. Technol. A* **23**, 593 (2005).
- [38] L. Zhou, D. Holec, and P. H. Mayrhofer, *J. Appl. Phys.* **113**, 043511 (2013).
- [39] R. Sanjinés, C. S. Sandu, R. Lamni, and F. Lévy, *Surf. Coat. Technol.* **200**, 6308 (2006).
- [40] S. Nikolov, M. Petrov, L. Lymperakis, M. Friák, C. Sachs, H.-O. Fabritius, D. Raabe, and J. Neugebauer, *Adv. Mater.* **22**, 519 (2010).
- [41] D. Ma, M. Friák, J. Neugebauer, D. Raabe, and F. Roters, *Phys. Status Solidi B* **245**, 2642 (2008).
- [42] P. Mayrhofer, D. Sonnleitner, M. Bartosik, and D. Holec, *Surf. Coat. Technol.* **244**, 52 (2014).